



# SAMURAI-S: Sonic Anemometer on a Multi-Rotor drone for Atmospheric turbulence Investigation in a Sling load configuration

Mauro Ghirardelli<sup>1</sup>, Stephan T. Kral<sup>1,2</sup>, Etienne Cheynet<sup>1</sup>, and Joachim Reuder<sup>1,2</sup>

<sup>1</sup>Geophysical Institute and Bergen Offshore Wind Centre, University of Bergen, 5020 Bergen, Norway.

<sup>2</sup>Bjerknes Centre for Climate Research, 5020 Bergen, Norway.

**Correspondence:** Mauro Ghirardelli (mauro.ghirdelli@uib.no)

**Abstract.** This study introduces the SAMURAI-S, a novel measurement system that incorporates a state-of-the-art sonic anemometer combined with a multi-rotor drone in a sling load configuration, designed to overcome the limitations of traditional mast-based observations in terms of spatial flexibility. This system enables the direct measurement of 3D wind vectors while hovering, providing a significant advantage in manoeuvrability and positional accuracy over fixed mast setups. The capabilities of the system are quantified through a series of 10 min to 28 min flights, conducting close comparisons of turbulence measurements at altitudes of 30 m and 60 m against data from a 60-meter tower equipped with research-grade sonic anemometers. The results demonstrate that SAMURAI-S matches the data quality of conventional setups for horizontal wind measurements while slightly overestimating vertical turbulence components. This overestimation increases as the wind speed increases.

## 1 Introduction

Since the 1960s, mast and tower-based sonic anemometry has been the standard for high-frequency turbulence measurements in atmospheric boundary layer (ABL) research (Foken, 2006; Mauder et al., 2021). With continuous technological development over the years, state-of-the-art sonic anemometers allow for in-situ flux estimations (e.g., Foken et al., 2012) and for the spectral characterization (e.g., Midjyawa et al., 2021) of turbulence. However, recent studies in ABL meteorology and wind energy, such as Fernando and Weil (2010), Mahrt (2014), or Veers et al. (2019), highlight the limitations of those traditional tower-based measurements, emphasizing the need for more flexible approaches to address a wider range of relevant ABL processes.

Some examples illustrating mast-based measurement limitations include the study of the coherence of turbulence (Cheynet et al., 2018), which is a critical design parameter for modern wind turbines. For such an investigation, it would be required to erect multiple 300-meter masts close to each other, which is impractical. The same holds for the detailed investigation of wind turbine wakes within a wind farm, as, e.g., explored by Porté-Agel et al. (2020), as variability in wind speed and direction make a proper positioning of masts in such dynamic conditions practically unfeasible. Other research topics that require alternative sensor carriers are the investigation of the wave boundary layer (Wu and Qiao, 2022), air-sea-exchange over the ocean (Taylor et al., 2018), and air-ice-sea interactions in polar regions, e.g., over open water areas within the sea ice (Marcq and Weiss, 2012).



25 Airborne platforms have been used to extend the range of turbulence-related measurements. Fixed-wing uncrewed aerial vehicles (UAVs), often employing multi-hole probes (Mansour et al., 2011; Wildmann et al., 2014a, b; Båserud et al., 2016; Witte et al., 2017; Calmer et al., 2018; Alaoui-Sosse et al., 2019; Rautenberg et al., 2019), have demonstrated their capability in turbulence sampling along the flight track across larger areas. The inability to hover or move very slowly is, however, restricting their ability for measurements in situations that require stationary point measurements or localized vertical profiling.

30 Conversely, tethered systems equipped with sonic anemometers can provide quasi-stationary measurements and are effective in vertical profiling (Ogawa and Ohara, 1982; Hobby, 2013; Canut et al., 2016). Those systems require, however, a considerable logistic effort and have clear operational limits with respect to wind speed and atmospheric turbulence that strongly affect their controllability. Consequently, tethered systems cannot be easily deployed in remote areas and complex terrain, or safely operated close to structures and buildings, e.g., in urban areas or the vicinity of wind turbines and wind farms.

35 Rotary-blade UAVs offer a more suitable sensor platform for localized and stationary measurements (Abichandani et al., 2020). Recent studies have explored the use of different methods of atmospheric flow measurements, by either using the drone's motion and attitude as a proxy for wind estimates (Segales et al., 2020; González-Rocha et al., 2020; Shelekhov et al., 2021; Wetz et al., 2021; Wildmann and Wetz, 2022), or by mounting of miniaturized sonic anemometers (Palomaki et al., 2017; Li et al., 2023) on the drone. Both methods show limitations for turbulence investigations due to the limited sampling frequency and, for most small sonic anemometers, the inability to measure the full 3D flow. First attempts of flying research-grade sonic anemometers (Hofsäß et al., 2019; Thielicke et al., 2021) have shown promising results with respect to the measurement of the mean wind speed, but full turbulence measurement capabilities are still unproven.

One main reason is that the propeller-induced flow (PIF) by the UAV can affect and disturb the on-board flow measurements. Mounting an extension arm, to place the wind sensor either to the front (Hofsäß et al., 2019), to the side, or above the drone (Thielicke et al., 2021) is one obvious possibility to minimize the PIF effect. As any mass outside the center of gravity of the UAV system will inevitably compromise flight stability and complicate flight control, it is necessary to thoroughly investigate and characterize the PIF for appropriate sensor placement considerations (Ghirardelli et al., 2023; Jin et al., 2024; Flem et al., 2024). The second option to mitigate the potential PIF influence on the measurements, without heavy impact on flight control and stability, is the deployment of the flow sensor as sling load under the drone.

45 Based on the latter concept, this study introduces SAMURAI-S as a novel measurement system for airborne atmospheric research using drones. Carrying the turbulence sampling payload 18 m under a rotary-wing UAV, the sensor is clearly located outside any measurable PIF effect (Flem et al., 2024). The payload consists of a research-grade sonic anemometer, an inertial navigation system (INS), a data acquisition unit, and a mounting frame. This design aims to overcome the above-mentioned limitations, thus providing state-of-the-art sonic anemometry data with the added benefits of mobility, hover capability, and adaptable positioning. This will enable detailed turbulence analysis in various settings, including observations close to structures and in urban environments where other methods fail.

This research aims to assess the accuracy and reliability of the developed measurement approach. The methodology involves a comparative analysis between traditional mast-mounted 3D sonic anemometers and the one suspended under the drone. Another key aspect of this study is to evaluate the applicability of a dynamic tilt and motion compensation algorithm to



60 account for the inevitable motion of the payload caused by wind drag and the drone's movements. This algorithm utilizes in-situ velocity and attitude data linked to the movement and orientation of the anemometer recorded by the INS. It aims to convert sonic anemometer turbulence measurements obtained from a moving platform into a natural wind or streamline coordinate system, as commonly used in ABL research.

The manuscript is organized as follows: Section 2 details the design of the UAV-payload system. Section 3 introduces the  
65 algorithm developed to account for the payload motion and it outlines the data post-processing techniques employed in the experimental comparison. Section 4 describes the experimental design for the system validation, including the measurement site and the setup of the mast instrumentation. Section 5 compares the integral and spectral flow characteristics derived from the mast- and drone-mounted sonic anemometers. This comparative study focused on various aspects of airflow, including mean flow and turbulence characteristics. Both integral and spectral flow characteristics were examined. Finally, Section 6  
70 summarizes the main findings of the study and concludes that SAMURAI-S provides a novel airborne instrument platform with a large potential for effectively measuring ambient turbulent flow with unprecedented flexibility.

## 2 The SAMURAI-S system

### 2.1 Airframe

Several important design criteria guided the selection of an appropriate airframe. Turbulence measurement with a drone-  
75 mounted sonic anemometer requires the ability to lift a payload of roughly 4 kg. This weight estimate results from the required components, i.e., a research-grade sonic anemometer, an inertial navigation system (INS), a battery, a data logger, and a mounting frame. A flight time of at least 15 min to 20 min is required for gathering turbulent flow time series that allow robust turbulence statistics for variances and covariances, as well as spectral analysis (Van der Hoven, 1957). Finally, to comply with European regulations for drone operations in the open category, we want to limit the UAV's maximum take-off weight  
80 (MTOW) to 25 kg, which also aids the logistical aspects of deploying the system in the field. At the same time, we considered flight safety, stability, and precision in positioning to be design priorities, since they are crucial across different real-world scenarios, e.g., operation in the proximity of infrastructures, human presence, or in complex environments.

To address these considerations, we opted for the Foxtech D 130 (Figure 1). This UAV has a nominal maximum payload of 20 kg and maximum flight time in hovering mode of up to 45 min without payload, depending on the atmospheric conditions. It  
85 is equipped with eight coaxial contra-rotating propellers, where four pairs of propellers, each driven by brushless electric motors, share the same rotational axis and are mounted on arms extending from the main body. The configuration of the propellers provides redundancy in case of a motor failure. The UAV's frame weighs approximately 9 kg. In its default configuration, it is powered by two 6S lithium polymer (LiPo) batteries, each with a capacity of 22 A h, resulting in a take-off weight of roughly 15 kg. The UAV has an onboard autopilot unit (Cubepilot Cube Orange) combined with 2 GNSS antennas (Here3). The UAV's  
90 specifications are shown in Table 1.

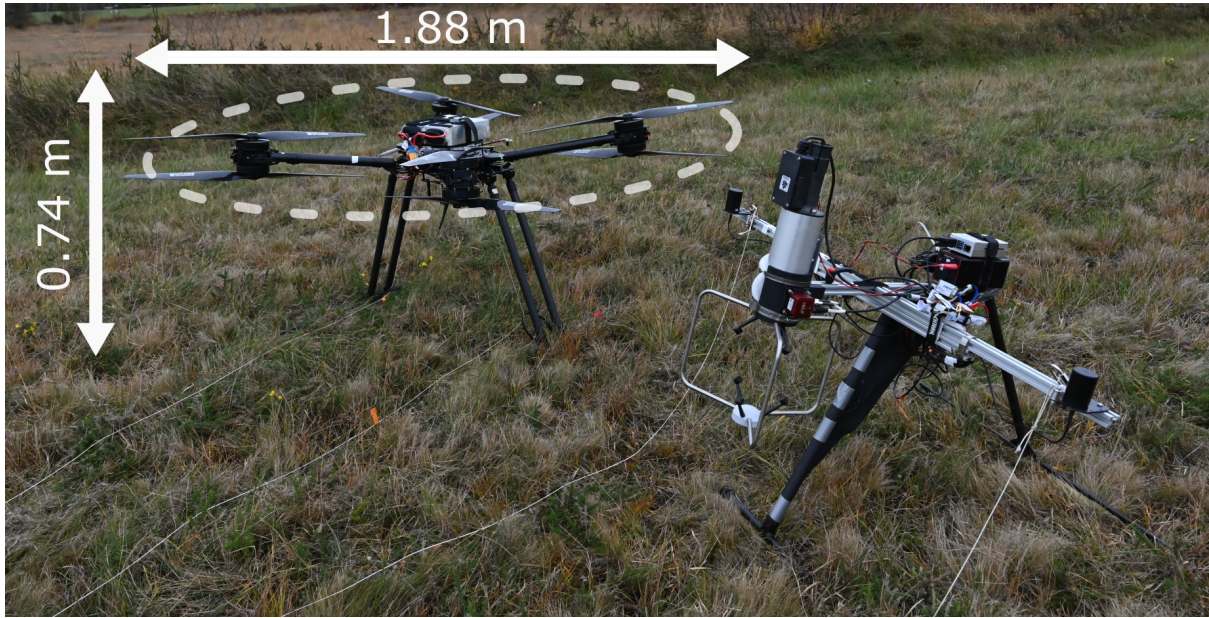


**Figure 1.** The SAMURAI-S UAS including UAV and payload.

## 2.2 Sensor placement

The placement of the sonic anemometer is critical for the quality of the turbulence observations, as it is proven that placing the sensor at a certain distance from the propellers effectively reduces the impact of the PIF (Prudden et al., 2016; Thielicke et al., 2021; Wilson et al., 2022). However, this approach requires an estimation of the volume significantly affected by the PIF, which varies with the UAV's geometry (Guillermo et al., 2018; Lei and Cheng, 2020; Lei et al., 2020). Moreover, the angular momentum resulting from the additional weight mounted outside the UAV's centre of gravity could significantly compromise flight stability.

To limit the influence of the PIF on the velocity measurements, sensors mounted on a boom above the mean rotor plane of UAVs have been used in the past (Palomaki et al., 2017; Shimura et al., 2018; Natalie and Jacob, 2019; Thielicke et al., 2021; Wilson et al., 2022). This mounting configuration is designed to achieve an evenly balanced weight distribution around the drone by aligning the sensor's weight with the UAV's vertical axis and centre of mass. Nevertheless, this point is true primarily in low wind conditions. In scenarios with stronger winds, the drone must tilt further to counteract the increased drag, affecting the initial balance and tilt angle. Finding the right boom length that effectively reduces PIF while maintaining the drone's manoeuvrability and determining its best orientation remains a subject of ongoing research.

Previous studies (Ghirardelli et al., 2023; Jin et al., 2024), based on the Foxtech D130, suggest the best trade-off between boom length and PIF reduction, while keeping the payload close to the UAV's fuselage, is achieved by positioning the boom upwind, with the sensor at the boom's end. This orientation avoids the areas significantly affected by the PIF as shown by Ghirardelli et al. (2023). However, to fully take advantage of this configuration, it is necessary to automatically align the sensor



**Table 1.** Specifications of Foxtech D130

Components	Characteristics
UAV diameter (m) × height (m)	1.88 × 0.74
UAV frame's weight (kg)	9
Propellers	Foxtech Supreme C/F 2880T
Propeller diameter (m) × pitch (m)	0.71 m × 0.20
Propeller's weight (g)	8 × 90
Battery	2 × 6S1P LiPo*
Battery's weight (kg)	2 × 2.4
Motors	T-Motor U10II**
ESC	T-Motor Flame 80A
Autopilot	Cubepilot Cube Orange***
GNNS	Here3 dual antenna
Flight Time (min)	40 to 45

\* 22 A h; 22.2 V; 30 C

\*\* 8.6 kg maximum thrust when paired to Foxtech Supreme C/F  
 Propeller 2880T

\*\*\* ArduCopter v4.3.6 in Aug and v4.4.3 in Dec

or UAV with the mean instantaneous wind direction, i.e. requiring an automatic flight control loop such as the "weathervaning"  
 110 algorithm recently implemented in ArduCopter v4.4.0 (see <https://ardupilot.org/copter/docs/weathervaning.html>) or through  
 adjustments in forward flight. To the authors' knowledge, a reliable prototype of this design has yet to be developed.

In this study, we adopt a novel approach, carrying the sonic payload platform as sling load 18 m under the drone, correspond-  
 ing to about 26 rotor diameters (D). This setup places the payload in a stable equilibrium state instead of mounting it above  
 the drone. When the payload is suspended beneath the drone, it creates a pendulum, swinging around the point of minimal  
 115 potential energy. This natural stability allows the payload to stabilize itself through its oscillations, reducing the need for the  
 drone to counteract these movements actively. The PIF features depend more on thrust rather than UAV's geometry in the far  
 field of the drone, i.e., in a distance of more than 5 D from the rotor plane, when the individual rotor downwash regions have  
 merged to one, (Ghirardelli et al., 2023; Flem et al., 2024). This should extend the applicability of the payload set-up to a wider  
 range of multi-copter platforms.

120 Simulations and observations were used to estimate the required vertical displacement of the wind sensor below the UAV. As  
 detailed in Ghirardelli et al. (2023), simulations within a domain extending 9.0 m below the drone, revealed that the ambient  
 wind effectively carries away the downdrafts. Notably, airflow closely resembled free-flow conditions at this domain's lower  
 boundary, directly under the drone and in conditions where wind speeds surpassed  $2.5 \text{ m s}^{-1}$ . This observation was further  
 supported by Jin et al. (2024), which utilizes a configuration of three CW Doppler LIDARs to measure the PIF generated

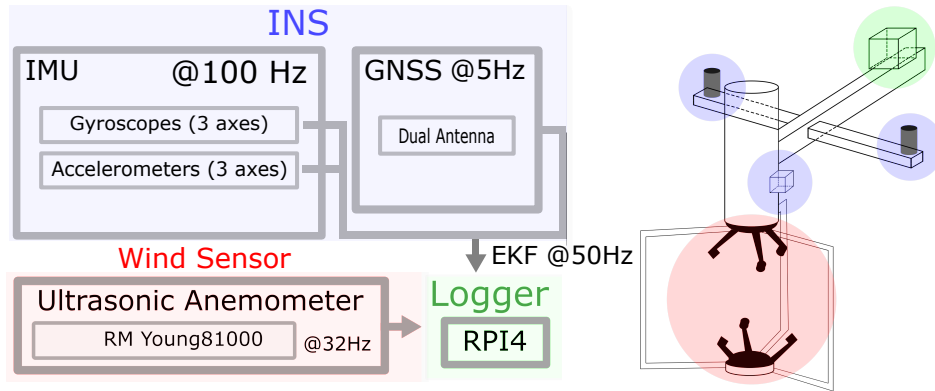


**Figure 2.** Diagram and blueprint of the measurement and acquisition system showing the data flow from the sensors to the logger.

125 by Foxtech D130 in hover. Measurements indicated negligible PIF distortion at a distance of 4.5 m below the Foxtech D130,  
 in an ambient flow of  $4.0 \text{ ms}^{-1}$ . Finally, Flem et al. (2024) showed how, for the same drone model and in the absence of a  
 background flow, the downdraft drops by more than 40 % in the range between 1.5 m to 6 m under the plane of the rotors. An  
 additional empirical confirmation can be derived from visual observations of a multi-rotor drone over the surface of a lake in  
 low wind conditions (Flem et al., 2024), showing that the PIF of the drone does not reach the surface with the UAV hovering at  
 130 a height of 15 D above the water. To add a margin of safety, we opted to double the distance identified in the CFD simulations.

### 2.3 Payload Description

The payload consists of an RM Young 81000 sonic anemometer, an SBG Eclipse-D inertial navigation system (INS) equipped  
 with two GNSS antennas, and a Raspberry Pi 4 microprocessor serving as a data logger (Figure 1 and Figure 2). The SBG  
 Eclipse-D is a compact INS featuring a dual-antenna GNSS receiver. It includes a MEMS-based Inertial Measurement Unit  
 135 (IMU) and uses an Extended Kalman Filter (EKF) to fuse inertial and GNSS data. Table 2 and Table 3 provide key specifications  
 of the sonic anemometer and the INS, respectively.

For the integration of the different sensors, the battery, and the data logger, we constructed a horizontal T-shaped aluminium  
 frame with a 0.55 m long main bar and a 1.00 m long crossbar. In addition, we added a T-shaped support leg to better protect  
 the sensors during landing, transport, and storage and a triangular wind vane to aid the sensor alignment with the mean wind  
 140 direction and dampen lateral and rotational oscillations around the yaw axis.

The sonic anemometer was mounted upside down in the front of this frame, with the INS attached via a custom-fitted  
 mounting plate to the side of its cylindrical support structure, assuring parallel alignment of both sensor coordinate systems.  
 The crossbar of the frame served as an attachment point for two nylon ropes used to link the payload to the sides of the UAV  
 and a 0.94 m long baseline for the two GNSS antennas mounted on the tips of the bar. The data logger and a battery were  
 145 positioned at the tail of the frame.



**Table 2.** Specifications of RM Young 81000 sonic anemometer.

Specifications	RM Young 81000
Wind Speed Range ( $\text{m s}^{-1}$ )	0 to 40
Wind Speed Resolution ( $\text{m s}^{-1}$ )	0.01
Wind Speed Accuracy ( $\text{m s}^{-1}$ , % RMSE)	$\pm 0.05$ , $\pm 1$ ,
Wind Dir. Elevation Range ( $^{\circ}$ )	$\pm 60.0$
Wind Dir. Resolution ( $^{\circ}$ )	0.1
Wind Dir. Accuracy* ( $^{\circ}$ )	$\pm 2$
Sonic Temp. Range ( $^{\circ}\text{C}$ )	$-50$ to $50$
Sonic Temp. Resolution (K)	0.01
Sonic Temp. Accuracy* (K)	$\pm 2$
Air Sample Path (m)	0.15
Output Rate (Hz)	4 to 32
Weight (kg)	1.7

\*  $0 \text{ m s}^{-1}$  to  $30 \text{ m s}^{-1}$  range

**Table 3.** Specifications of the SBG Ellipse-D inertia navigation system with RTK aiding for airborne applications

Specifications	Ellipse-D*
Horizontal position accuracy	0.01 m
Vertical position accuracy	0.02 m
Horizontal velocity accuracy	$0.03 \text{ m s}^{-1}$
Vertical velocity accuracy	$0.03 \text{ m s}^{-1}$
Pitch and Roll accuracy	$0.05^{\circ}$
Heading accuracy	$0.4^{\circ}$
Weight INS (including GNSS antennas)	0.3 kg

\* data were logged using the sbgBasicLogger program (sbgECom library v3.2.4011, <https://github.com/SBG-Systems/sbgECom>)

The attachment points for the ropes are aligned with the pitch axis of both the UAV and the sling load (SL) frame. The entire payload system was balanced for the sonic anemometer's pitch by shifting the position of the crossbar as well as the battery and data logger. The roll motion is directly transferred to the sonic anemometer from the drone in contrast to the yaw motion, while the pitch depends solely on the balance of the payload. Although the drone-payload setup behaves like a compound pendulum due to the two suspension ropes attached to the same weight (the payload), it has been treated as a simple



pendulum for simplicity. The natural oscillation period ( $T$ ) is estimated using the formula  $T = 2\pi\sqrt{\frac{l}{g}}$ , where  $l$  is the length of the ropes, and  $g = 9.81 \text{ ms}^{-2}$  is the gravitational acceleration. This calculation yields an oscillation period of approximately 8.5 s, corresponding to a frequency of 0.12 Hz. Preliminary analysis of the sonic data, conducted before performing the motion compensation, consistently reveals a distinct peak at this frequency across all flights.

### 155 3 Payload data processing workflow

This section outlines the methodological approach to convert the raw flow data sampled by the payload into the natural wind vector expressed in the standard meteorological coordinate system. One primary challenge is the handling of asynchronous raw sensor outputs expressed in different coordinate frames. In addition, it is necessary to compensate the measurements for the motion of the payload. The workflow herein presented addresses both points through a three-stage process: first, the sonic  
160 and INS outputs are filtered to remove faulty data and outliers, enhancing their quality and reliability. Next, INS and sonic output are synchronized, creating a unified temporal framework. Finally, dynamic rotational and translatory transformations are applied to account for changes in the orientation of the payload and its movements, which primarily come from swinging motions during hovering. For clarity, we first introduce the reference systems that describe the coordinates in which the data are collected and the rotations performed.

#### 165 3.1 Wind vector, coordinate frames and transformation

We define two right-handed coordinate systems to describe the motion of the payload: the inertial frame and the body frame, denoted by the indices  $\mathbf{i}_n$  and  $\mathbf{b}_n$  ( $n = 1, 2, 3$ ), respectively. The inertial (or NED) frame is Earth-fixed, and its axes ( $i_1, i_2, i_3$ ) are oriented northward, eastward, and downward, respectively (Figure 3a). The body frame is centred at the sonic anemometer's sampling volume and moves along with the payload. Its axes are defined based on the geometry of the payload, with  $b_1$  pointing  
170 forward,  $b_2$  to the right side, and  $b_3$  downward (e.g., Palomaki et al. 2017). Its orientation (attitude) and movements relative to the inertial frame can be described by the Euler angles and the velocity vector measured by the INS, respectively (Figure 3b).

To transform the raw flow measurements from body frame coordinates ( $\mathbf{V}_b$ ) to inertial frame coordinates ( $\mathbf{V}_i$ ), a rotation matrix  $R(\phi, \theta, \psi)$  is applied (Beard and McLain, 2012; Wetz et al., 2021). This matrix, defined by the roll, pitch, and yaw angles ( $\phi$ ,  $\theta$ , and  $\psi$ ), adjusts the raw wind vector to reflect the orientation of the payload relative to the inertial frame, and  
175 is fully detailed in Appendix A. By subtracting the relative velocity vector  $\mathbf{V}_i^b$ , accounting for the movement of the body frame relative to the inertial frame, it is in addition possible to eliminate any component of the velocity due to the motion of the payload, isolating the natural wind vector in the inertial frame. The equation that accounts for both of these dynamic corrections is expressed as:

$$\mathbf{V}_i = R(\phi, \theta, \psi)\mathbf{V}_b - \mathbf{V}_i^b \quad (1)$$

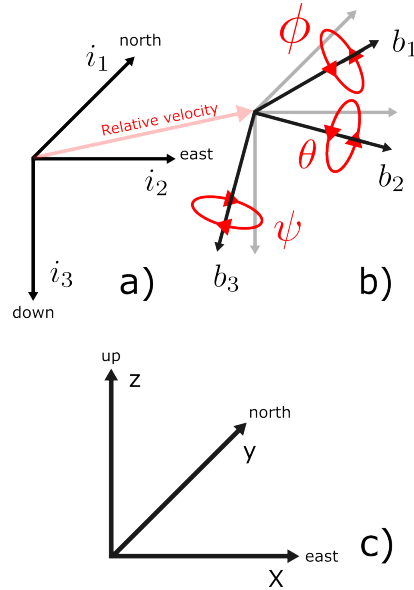


**Figure 3.** Panel (a) illustrates the inertial frame (NED), where the axes  $i_1$ ,  $i_2$ , and  $i_3$  point northward, eastward, and downward, respectively. Panel (b) depicts the body frame centred at the sonic anemometer’s sampling volume, with axes  $b_1$ ,  $b_2$ , and  $b_3$  pointing forward, to the right, and downward. This panel also includes the Euler angles  $\phi$ ,  $\theta$ , and  $\psi$  depicting the orientation of the body frame relative to the inertial frame, along with the relative velocity vector  $\mathbf{V}_i^b$ . Panel (c) shows the meteorological frame used to represent the wind vector  $\mathbf{U}$ , with axes oriented eastward, northward, and upward.

180 A final orthogonal rotation by right angles is performed to retrieve the wind vector ( $\mathbf{U}$ ) in the standard meteorological coordinate frame, the natural wind coordinate system, with  $x$ ,  $y$ , and  $z$  pointing east, north, and up, respectively (Figure 3c).

$$\mathbf{U} = \begin{pmatrix} 0 & 1 & 0 \\ 1 & 0 & 0 \\ 0 & 0 & -1 \end{pmatrix} \mathbf{V}_i \quad (2)$$

### 3.2 Data filtering

The sonic anemometer, providing the three wind velocity components and the sonic temperature, was set to a sampling frequency of 32 Hz. Each data instance is timestamped according to the Raspberry Pi internal clock. Since the Raspberry Pi does not have a GNSS signal, the internal clock does not necessarily correspond to exact UTC. Therefore, these time stamps are converted to  $\mu\text{s}$  from the start of the logging interval, using the first recorded timestamp as an offset. In addition, the time series were adjusted to account for the upside-down mounting orientation of the sonic anemometer, ensuring that the measured vectors were appropriately rotated in the body frame coordinates before processing.

190 The raw INS output consists of 100 Hz IMU data and 5 Hz GNSS data. The IMU provides angular rates (gyroscope data) and accelerations (accelerometer data), while the GNSS supplies the local velocity, latitude, longitude, altitude, and roll and yaw



angles. Furthermore, the INS outputs Kalman-filtered (EKF) data at 50 Hz, fusing inputs from both GNSS and IMU. It consists of 3D velocity data and Euler angles, both given in the NED inertial frame, as well as latitude, longitude and altitude data. Given the prototype nature of the developed system, the data processing was exclusively based on the EKF output (Table 3).

195 Moreover, the SBG Ellipse-D INS allows to output position, velocity and attitude data at a geometrically specified location relative to the sensor. For convenience, we thus configured the INS to output data in the body frame centred on the sonic anemometer measurement volume. Each data point from the INS is timestamped with the INS internal time in ns from the start of the data log and in UTC post-GNSS signal acquisition. Figure 2 shows a schematic representation of the payload system.

As an initial filter, we removed all data collected before establishing a valid and stable GNSS time. Following this, data points exceeding the measurement range of the instruments were discarded from further analysis. The filtering thresholds were determined based on the sensor specifications provided by the manufacturers. Additionally, following a despiking method adopted from Mauder et al. (2013), outliers were removed using a moving absolute deviation (MAD) filter relying on a sliding window of 10 s and a distance of  $\pm 7$  MAD from the median. Missing or flagged data accounted for less than 2 % of all the collected data for each individual flight. Thus, they were filled using linear interpolation. The third and final step of the filtering process consisted of identifying the time windows corresponding to the hovering state of the drone. This involved a two-step filtering approach. Initially, a filter was applied based on the median altitude  $\pm 3$  m, followed by a  $\pm 4$  m median filter on horizontal movements to address horizontal swinging. Finally, the EKF output is then downsampled to 32 Hz to match the sampling frequency of the sonic anemometer.

### 3.3 Data synchronization and coordinates transformation

210 Ensuring accurate synchronization between the INS and the sonic anemometer outputs is crucial for correctly applying Equation (1), designed to compensate for payload motion during flight. To address potential synchronization discrepancies, we implemented an iterative process that involves progressively changing the time lag of the sonic anemometer relative to the INS within a range of  $\pm 2$  s, with each step corresponding to  $1/32$  s. At each adjustment step, Equation (1) is applied to the sonic data, and we calculate the mean turbulent kinetic energy (TKE) from the resulting time series. Notably, the TKE as a function of the time lag consistently shows a reverse bell shape with the minimum located between  $-0.185$  s to  $0$  s, as shown in Figure 4. Apart from the location of the time lag, this figure also indicates that potential errors associated with an imperfect time-lag correction, e.g. by a few time increments, would result in small relative errors in the computed TKE.

The time series adjusted using the time lag that minimizes the TKE are selected for further analysis. This selection is based on the assumption that the payload movement is most effectively compensated at this optimal lag. Finally, these time series are transformed into natural wind coordinates using Equation (2).

## 4 Data and methods for the validation experiment

The validation study was conducted at the Plateforme Pyrénienne d’Observations Atmosphériques (P2OA) in Lannemezan, southwestern France, during two special observation periods in August and December 2023, as part of the Model and Ob-

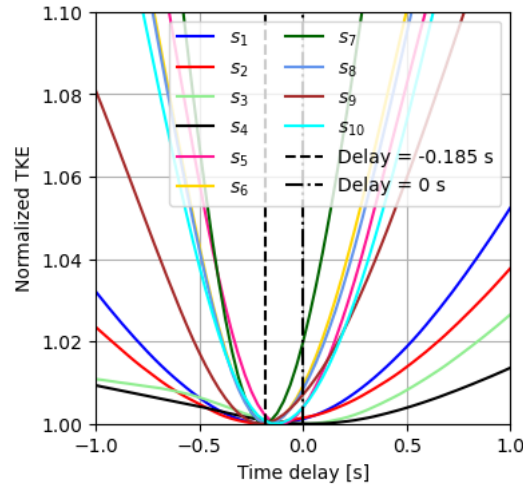


**Figure 4.** Normalized Turbulent Kinetic Energy (TKE) curves across validation flights (named  $s_1$  to  $s_{10}$ ) plotted as a function of time delay (in seconds) of the sonic anemometer output relative to the INS output. Each TKE profile is normalized by its minimum value to facilitate direct comparisons. Vertical lines at  $-0.185$  s (dashed line) and  $0$  s (dash-dot line) indicate the time window where all minimum values are located. The axes limits are set to  $-1$  to  $1$  for the x-axis and  $1$  to  $1.1$  on the y-axis to highlight subtle differences among the profiles.

225 observation for Surface Atmosphere Interactions (MOSAI) campaign. These periods featured the deployment of reusable ra-  
 diosondes, multiple eddy-covariance stations, meteorological masts, and various remotely piloted aircraft systems, including  
 the SAMURAI-S, for a suite of measurements dedicated to studying the effects of surface heterogeneities. Additionally, a  
 tethered balloon equipped with a sonic anemometer (Canut et al., 2016) provided a complementary method for assessing atmo-  
 spheric turbulence. While this constitutes an important experimental dataset, the current work focuses solely on the validation  
 of the SAMURAI-S system. Detailed analysis of the scientific data from the experimental campaign is reserved for future  
 230 publications.

The P2OA observatory is located in a rural and heterogeneous area, primarily characterized by agricultural fields and forests,  
 with a typical length scale of  $500$  m (e.g., BLLAST Lothon et al., 2014). The site is equipped with a  $60$ -meter meteorological  
 tower featuring a triangular lattice structure (Figure 5). The surrounding terrain is predominantly flat and characterized by a  
 heterogeneous mix of grazing land, grasslands, crop fields, and forest. Within  $1$  km of the  $60$ -meter tower, grasslands are more  
 235 prevalent. The tower is equipped with slow-response sensors for temperature, humidity, wind speed, and direction at five levels  
 ( $2$  m,  $15$  m,  $30$  m,  $45$  m and  $60$  m) and eddy-covariance systems at three levels ( $30$  m,  $45$  m and  $60$  m), of which only the lower-  
 and uppermost system were operational during our validation period. The two Campbell Scientific CSAT3 sonic anemometers  
 are mounted on horizontal booms on the tower at heights of  $30$  m and  $60$  m meters above the ground ( $633$  m and  $663$  m above  
 mean sea level), with an orientation of  $218.0^\circ$  and  $230.5^\circ$ , respectively. These anemometers are operated with a sampling  
 240 frequency of  $10$  Hz, recording the three velocity components and the sonic temperature. The validation study described herein  
 comprises several hovering flights of SAMURAI-S at target altitudes of  $30$  m and  $60$  m, in close proximity to the mast.

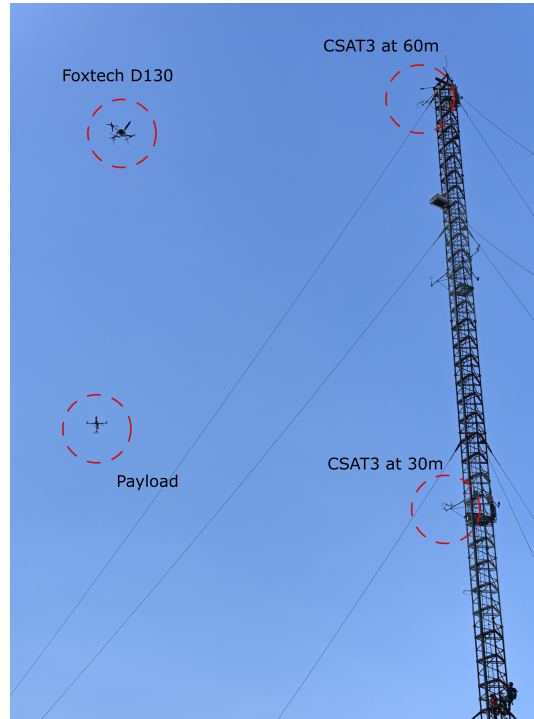


**Figure 5.** SAMURAI-S hovering side-by-side with the reference mast. The two CSAT sonic anemometers are mounted at 30 m and 60 m agl, oriented towards  $218.0^\circ$  and  $230.5^\circ$ , respectively.

#### 4.1 Tower validation study: theoretical framework

For this validation study, we employ an additional coordinate transformation, expressing the wind vector  $\mathbf{U}$  in streamlined coordinates with the three velocity components ( $u$ ,  $v$ , and  $w$ ), corresponding to the along-wind, cross-wind, and vertical (upward) directions, respectively (Kaimal and Finnigan, 1994). We apply Reynold decomposition, splitting each component  $i = u, v, w$  in its mean,  $\bar{i}$ , and a fluctuating part,  $i'$ . The standard deviations of the  $u$ ,  $v$ , and  $w$  components are represented by  $\sigma_u$ ,  $\sigma_v$ , and  $\sigma_w$ . Additionally, the skewness and kurtosis of these components are denoted by  $\gamma_i$  and  $\kappa_i$ .

This study utilizes the blunt and pointed spectral models (Olesen et al., 1984; Tieleman, 1995) to examine whether the velocity spectra conform to the  $-5/3$  power law in the inertial subrange. The models are expressed dimensionless as follows:



$$250 \quad \frac{f S_u(f)}{u_*^2} = \frac{a_u f_r}{(1 + b_u f_r)^{5/3}} \quad (3)$$

$$\frac{f S_v(f)}{u_*^2} = \frac{a_v f_r}{(1 + b_v f_r)^{5/3}} \quad (4)$$

$$\frac{f S_w(f)}{u_*^2} = \frac{a_w f_r}{1 + b_w f_r^{5/3}} \quad (5)$$

$$\frac{f \text{Re}(S_w(f))}{u_*^2} = \frac{a_{uw} f_r}{(1 + b_{uw} f_r)^{7/3}} \quad (6)$$

where  $f_r = \frac{fz}{u}$  represents the reduced frequency, while  $a_i$  and  $b_i$ , with  $i = \{u, v, w, uw\}$ , are coefficients empirically determined.  
 255

The Obukhov length (Monin and Obukhov, 1954) can be calculated as

$$L = - \frac{u_*^3 \bar{\theta}_v}{g \kappa (\overline{w' \theta'_v})} \quad (7)$$

where  $\bar{\theta}_v$  is the mean virtual potential temperature approximated by the sonic temperature,  $\kappa = 0.40$  is the von Kármán constant, and  $\overline{w' \theta'_v}$  is the vertical kinematic flux of virtual potential temperature. The nondimensional stability parameter  $\zeta$  is  
 260 defined as  $\zeta = z/L$ , where  $z$  is the height above the surface.

Following Kolmogorov's hypothesis of local isotropy in the inertial subrange, the spectral ratios  $S_w/S_u$  and  $S_v/S_u$  should converge toward 4/3 as the frequency increases (Busch and Panofsky, 1968; Kaimal et al., 1972). To compare the effectiveness of the mast-mounted and drone-mounted sonic anemometers in resolving turbulence with minimal flow distortion, we apply a quadrant analysis based on the comparison of the ratio  $S_w/S_u$  between the two sensor configurations (Figure 6). In the ideal  
 265 scenario, data points in this figure would cluster around the centre of the plot, as the 4/3 ratio is reached by both the drone and mast-based data. Deviations from this ratio could indicate flow distortion caused by the supporting structure, the sensor head, or both (Cheynet et al., 2019; Peña et al., 2019). A spectral ratio approaching but not reaching 4/3 may suggest that isotropy in the inertial subrange is not achieved within the investigated frequency range (Chamecki and Dias, 2004). A spectral ratio that plateaus without reaching the 4/3 law may reflect flow distortion, typically manifesting as an underestimation of the vertical  
 270 velocity component. It should be noted that Kolmogorov's hypothesis of local isotropy in the inertial subrange may not apply under non-stationary conditions, e.g., in very stable atmospheric conditions with intermittent turbulence. Thus, the quadrant analysis was conducted only for samples with a mean wind speed above  $2 \text{ m s}^{-1}$ , which was sufficient in this study to eliminate samples that did not exhibit characteristics consistent with the framework adopted here to describe turbulence.

In this study, the spectral ratios are studied using a limited frequency range of interest, which is computed using the reduced  
 275 frequency  $f_r = fz/\bar{u}$ , and  $f_r > 2$  following Kaimal et al. (1972). An upper boundary  $f_r < 10$  is also applied to ensure a fairer comparison between the drone and mast data.

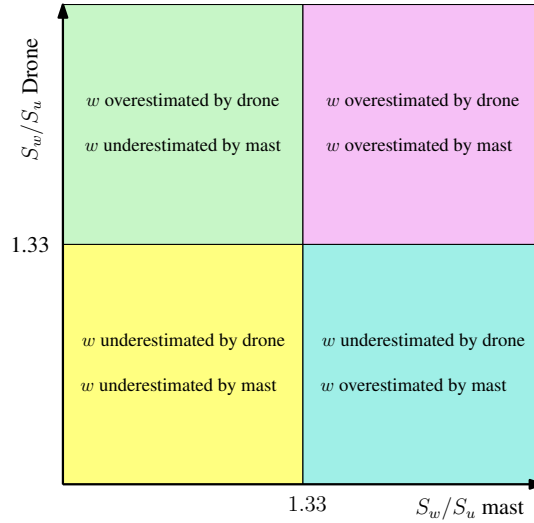


**Figure 6.** Quadrant analysis of the spectral ratios  $S_w/S_u$  to identify which sensor configuration may overestimate or underestimate the vertical velocity component. For brevity, "drone" refers to the drone-mounted sonic anemometer in this figure, and "mast" refers to the mast-mounted sonic anemometer.

## 4.2 Data processing

The processed data from the payload and those from mast-mounted anemometers are initially synchronized using the cross-correlation function between the horizontal velocity fluctuations. This aligns the time series of horizontal velocity, correcting any time lags up to 6 s through linear interpolation. Subsequently, the data are decimated by a factor of 4, and an anti-aliasing finite impulse response (FIR) filter of order 4 is applied. This leads to a sampling frequency of 8 Hz, which was adequate for properly comparing the two datasets.

Misalignments could occur when mounting the sonic anemometer on the tower or between the INS and the sonic anemometer on the payload. To detect such discrepancies, the datasets from both the payload and the mast (set as the reference) are compared after retrieving the velocity components—namely  $u$ ,  $v$ , and  $w$ —using single, double, or triple rotation methods. While the single rotation aligns  $u$  with the mean wind direction, the double-rotation method involves an additional pitch rotation, ensuring  $\overline{w} = 0$ . In contrast, the triple rotation includes a third rotation around the roll axis to ensure the crosswind component of the kinematic momentum flux ( $\overline{v'w'}$ ) becomes zero. A preliminary comparison involving these three rotations showed limited differences, demonstrating the suitability of the measurement setup. Therefore, the double-rotation method was chosen for both the mast-mounted and the drone-mounted anemometers for further analysis.

Integral and spectral turbulence characteristics are studied using linearly detrended data. Auto (PSD) and cross-power spectral densities (CPSD) of the velocity and temperature fluctuations are estimated using Welch's method (Welch, 1967). This involves segmenting the data into three parts with 50% overlap. An additional step includes smoothing the PSDs by bin-averaging them over 100 logarithmically-spaced bins (Kaimal and Finnigan, 1994).



**Table 4.** Summary of the ten samples assessed in this study.

Sample ID	Starting Time (UTC)	Duration (min)	Mean wind Direction (°) *	Payload height (m) **	Wind Speed (m s <sup>-1</sup> ) *	Stability parameter $\zeta$ (°) *
$s_1$	21-Aug-2023 14:05:32	28.0	97	28	3.1	-0.46
$s_2$	07-Dec-2023 12:33:52	18.7	277	27	0.8	0.38
$s_3$	07-Dec-2023 13:15:26	17.6	265	50	0.4	0.32
$s_4$	07-Dec-2023 15:08:09	17.8	277	57	0.6	1.25
$s_5$	08-Dec-2023 15:09:53	10.6	282	56	7.4	0.07
$s_6$	13-Dec-2023 07:27:17	18.3	300	48	8.2	0.2
$s_7$	13-Dec-2023 07:53:37	15.3	304	49	10.4	0.1
$s_8$	13-Dec-2023 08:37:11	15.3	310	23	7.1	0.20
$s_9$	13-Dec-2023 09:54:21	16.5	298	26	6.5	0.01
$s_{10}$	13-Dec-2023 10:19:58	20.2	296	49	7.1	0.05

\* Value estimated by the mast-mounted sonic anemometer closest to the payload height during the hovering window

\*\* Average height of the drone during the hovering window.

## 295 5 Results and discussion

In this study, we examine a data set comprising ten samples, labelled  $s_1$  to  $s_{10}$  in Table 4, to assess turbulence measurements obtained via the drone-mounted sonic anemometer. These samples were chosen from 17 initial flights, with the selection criteria based on at least 10 min of continuous, high-quality EKF output corresponding to hovering flight. Notably,  $s_2$ ,  $s_3$ , and  $s_4$  have mean flows of less than  $2 \text{ m s}^{-1}$ . The assumptions of turbulence being stationary, homogeneous, ergodic, and modelled as a Gaussian random process might not hold for these flights. For this reason, they are not subjects of the quadrant analysis, the framework of which is presented in Section 4.1. Nevertheless, they are included in the rest of the analysis for completeness. Figure 7 shows the associated altitude of the payload above the ground (left panel) and the hovering distance from the tower during the measurement periods (right panel).

Although all flights were analyzed, for brevity, Section 5.1 features a detailed comparison of the exemplary cases from sample  $s_1$  and  $s_7$  as they exhibit markedly different characteristics. Sample  $s_1$  targeted a height of 30 m and features convective conditions ( $\zeta = -0.46$ ) with rather weak wind of  $3.1 \text{ m s}^{-1}$ . Conversely, sample  $s_7$ , which targeted 60 m, is characterized by stable stratification conditions ( $\zeta = 0.1$ ) and the highest wind speed in the series ( $10.4 \text{ m s}^{-1}$ ). It will be shown that while  $s_1$  exhibits an excellent correlation between the drone-mounted anemometer and its mast-mounted counterpart,  $s_7$  presents some discrepancies in the vertical component when comparing the two anemometers. Following these detailed examinations, we systematically compare all samples based on their integral flow characteristics in Section 5.2.

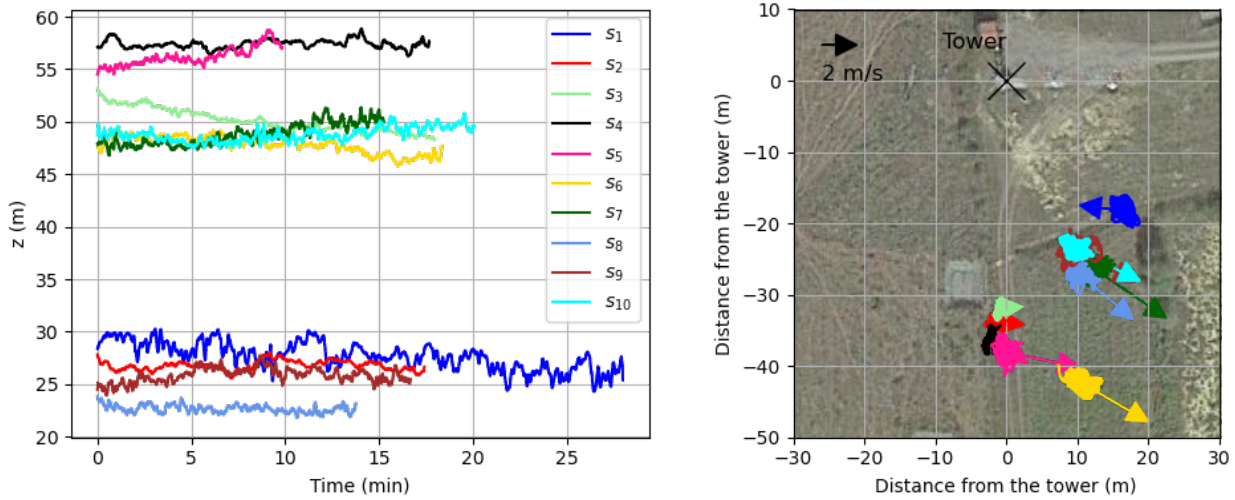


**Figure 7.** Drone altitude (left panel) and horizontal position relative to the tower (right panel) during the measurement periods of the ten validation flights. The sonic anemometers on the mast are mounted at heights of 30 m and 60 m, oriented at  $218^\circ$  and  $230.5^\circ$ , respectively. Wind directions for each flight are shown as coloured arrows, originating from the average horizontal positions. The arrow lengths correspond to a reference vector of  $2 \text{ m s}^{-1}$ . Imagery ©2024 Maxar Technologies, Map data ©2024 Google

### 5.1 Cases of samples $s_1$ and $s_7$

This section focuses first on the second-order structure of turbulence (i.e., variances and covariances) of  $s_1$  and  $s_7$ , though the third and fourth statistical moments are also briefly discussed for completeness. Results related to temperature are presented separately later in the section. Figure 8 presents time series of the velocity components  $u$ ,  $v$ , and  $w$  for samples  $s_1$  and  $s_7$ .  
 315 Table 5 expands further on this comparison by showing the statistical moments for the three velocity components between the reference mast data and the SAMURAI-S data.

The data exhibit a clear similarity, with no noticeable deviations except for the vertical velocity component  $w$  of sample  $s_7$ , where the drone-mounted sonic anemometer shows slightly larger fluctuations ( $\sigma_w = 1.3 \text{ m s}^{-1}$ ) than those from the mast-mounted sensor ( $\sigma_w = 1 \text{ m s}^{-1}$ ). All three velocity components in the mast and the payload data exhibit skewness and kurtosis  
 320 values close to zero and three, respectively. These measurements indicate Gaussian fluctuations, typically observed in stationary conditions within the ABL. Despite a 11 m altitude discrepancy between the sensors (see Figure 7), the drone-mounted sensor accurately tracks short-term horizontal velocity fluctuations. The altitude difference is primarily due to the UAV's altitude control being based on pressure rather than GNSS. Unfortunately, this discrepancy was only noticed during the post-processing phase and was not corrected in the field.

325 Figure 9 presents the auto power spectral density (PSD) for each velocity component and the real part of the cross-spectrum between  $u$  and  $w$  for samples  $s_1$  and  $s_7$ , plotted on a log-log scale and multiplied by the frequency  $f$  to highlight spectral features. The smooth PSD is computed using Equations (3) to (6) that is fitted to the data recorded by the payload sensor. This

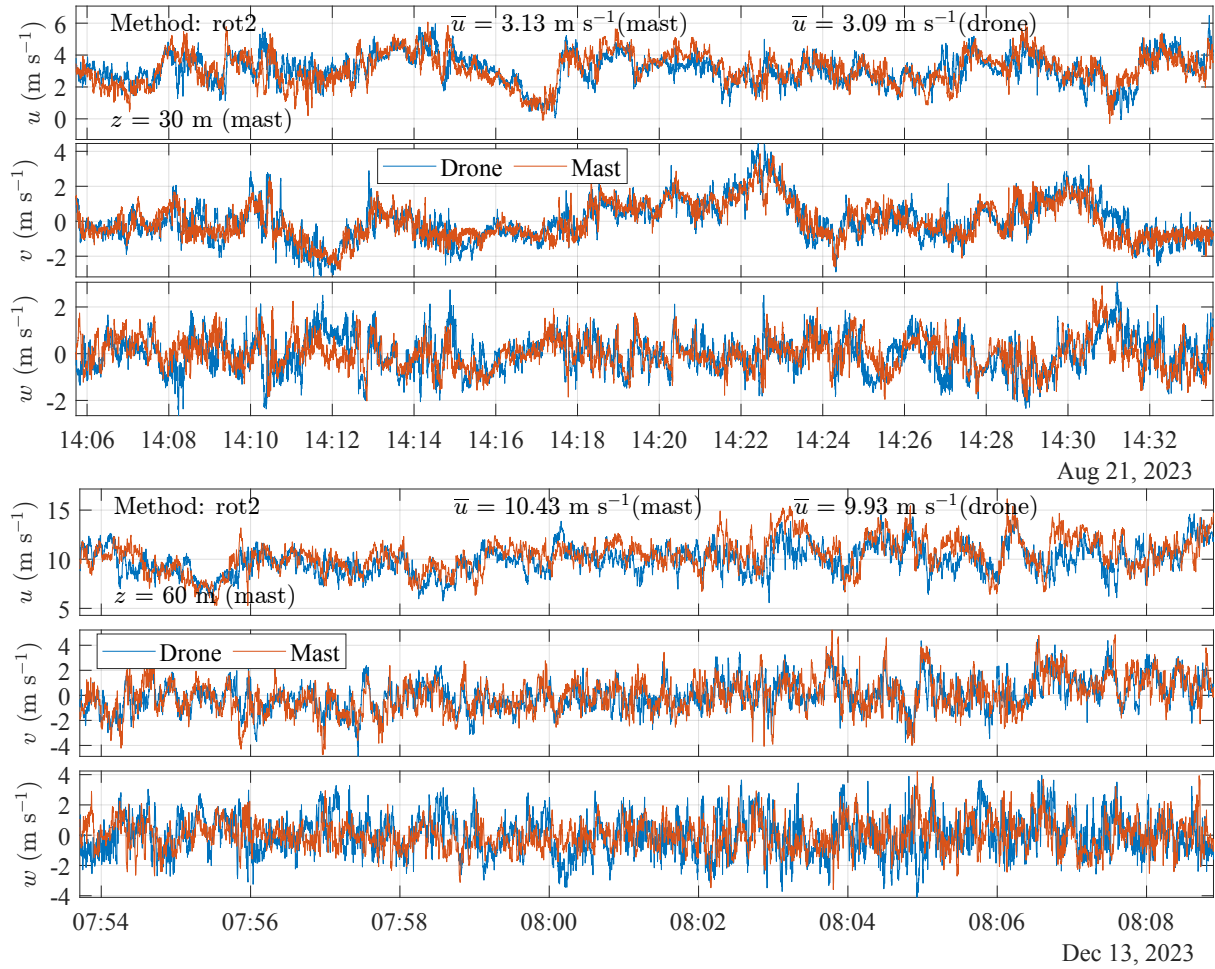


**Figure 8.** Velocity time series from the drone flights  $s_1$  (upper panel) and  $s_7$  (lower panel) where the SAMURAI-S anemometer is located near the 30-m sonic (samples  $s_1$ ) and the 60-m sonic (sample  $s_7$ ).

least-square fit is useful to assess whether the estimated PSD follows the  $-5/3$  power law associated with the inertial subrange for the  $S_u$ ,  $S_v$ , and  $S_w$  spectra, and the  $-7/3$  power law for the co-spectrum  $\text{Re}(S_{uw})$ . A slightly steeper roll-off is observed for the mast data.

Both sensors consistently capture the along-wind ( $u$ ) and across-wind ( $v$ ) velocity components for the selected samples  $s_1$  and  $s_7$ . In sample  $s_1$ , the  $S_v$  spectrum reveals a small peak at approximately 0.20 Hz. This peak cannot be attributed to the oscillation frequencies of the payload, which are established around 0.11 Hz. Thus, it is more likely related to a real flow feature. The co-spectrum between  $u$  and  $w$  for sample  $s_1$  features unusual positive values in the mast-mounted data between 0.03 Hz to 1 Hz, with a distinctive positive peak at 0.04 Hz. These features are not present in the SAMURAI-S data, indicating



**Table 5.** Statistical moments for samples  $s_1$  and  $s_7$  for drone and mast Data. Samples  $s_1$  and  $s_7$  refer to the samples described in Table 4.  $\sigma_i$ ,  $\gamma_i$ , and  $\kappa_i$ , where  $i = u, v, w$ , refer to the standard deviation, skewness, and kurtosis estimates, respectively.

Statistic	Sample $s_1$		Sample $s_7$	
	Drone Data	Mast Data	Drone Data	Mast Data
$\bar{u}$ (m s <sup>-1</sup> )	3.1	3.1	9.9	10.4
$\sigma_u$ (m s <sup>-1</sup> )	0.9	1.0	1.4	1.5
$\sigma_v$ (m s <sup>-1</sup> )	1.1	1.0	1.2	1.3
$\sigma_w$ (m s <sup>-1</sup> )	0.8	0.7	1.3	1.0
$\gamma_u$	-0.2	-0.2	0.0	-0.1
$\gamma_v$	0.4	0.4	0.1	0.0
$\gamma_w$	0.0	0.3	0.2	0.3
$\kappa_u$	3.0	2.7	2.8	3.0
$\kappa_v$	3.4	2.8	3.2	3.3
$\kappa_w$	2.8	3.4	2.8	3.4

differences in the flow between those captured by the tower-mounted instrument. This peak is unlikely related to a shadow effect of the tower, given that the wind direction was 97° and the tower-mounted sonic sensor is oriented towards 218° for  $s_1$ .

For flight  $s_7$ , the power spectral density of the vertical component clearly shows a higher energy content at all frequencies recorded by the drone-based sonic anemometer compared to those from the tower (Figure 9). This feature is present in nearly all flights (see Section 5.2), although it is particularly pronounced in  $s_7$ .

The comparative analysis of the sonic temperature time series reveals a good agreement across sample  $s_1$  and  $s_7$ , with minor deviations for the mean temperature likely attributable to different calibration values between the sonic anemometers (Figure 10). Further insights are provided by Figure 11, which displays the PSD estimates of the sonic temperature and the CPSD between the vertical and the along wind component with the virtual potential temperature. Notably, the PSD for sample  $s_1$  demonstrates an excellent agreement between the sonic temperature from the mast-mounted sensor and SAMURAI-S. However, for sample  $s_7$ , the PSD of the drone-based anemometer deviates from the expected  $-5/3$  power law at frequencies greater than 1 Hz. This deviation scales with frequency  $f$ , suggesting the influence of white noise on the measurement data. For the mast-mounted anemometer, the PSD estimates of the temperature exhibit slight discrepancies from this  $-5/3$  power law in samples  $s_1$  and  $s_7$ .

## 5.2 Comprehensive comparison

A comprehensive analysis of the sensor performance is conducted in this section, focusing on integral mean flow and turbulence characteristics for all three velocity components  $u$ ,  $v$ , and  $w$  (Figure 12) for all ten samples. Figure 13 compares the covariance-based kinematic momentum, heat fluxes, and stability estimated from the SAMURAI-S and the mast-mounted anemometer.

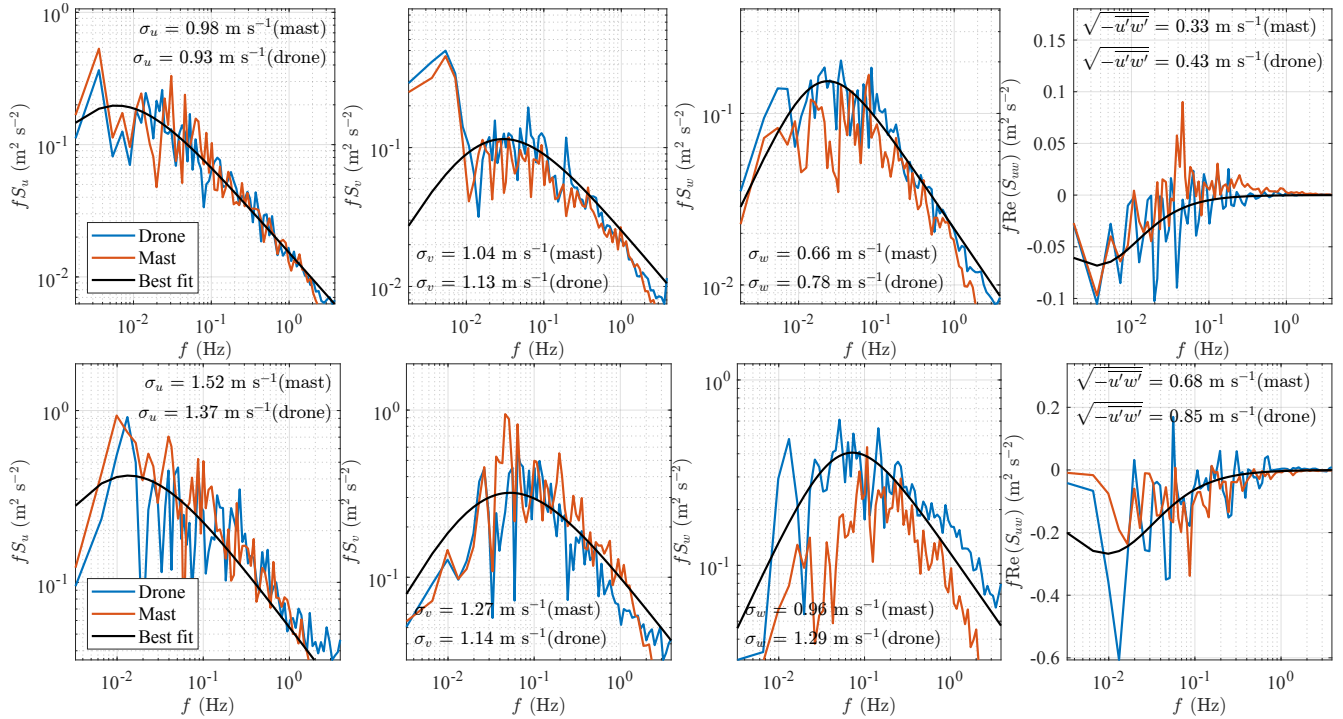


**Figure 9.** Power spectral density estimates of the velocity components for both the flying sonic anemometer and the one mounted on the mast at a height of 30 m above the ground for samples  $s_1$  (top) and the one mounted at 60 m for  $s_7$  (bottom). The solid black line refers to the blunt model (for  $S_u$ ,  $S_v$ , and  $S_{uw}$ ) or pointed model (for  $S_w$ ) fitted to the data from the drone-mounted anemometer.

The drone-mounted anemometer slightly underestimates the mean wind speed  $\bar{u}$  (Figure 12a), but the data scatter is low. This underestimation is possibly due to differences in height, since, as it is shown in Table 4, the payload height was on average 4 m lower than the target altitude for the sonic at 30 m and 8.5 m for the sonic at 60 m. The standard deviations of the along-wind and across-wind velocity components denoted  $\sigma_u$  (Figure 12b) and  $\sigma_v$  (Figure 12c), respectively, show excellent agreement. The drone-mounted anemometer slightly overestimates the standard deviation  $\sigma_w$  of the vertical component (Figure 12d), and this overestimation increases with the mean wind speed in absolute terms.

The covariance estimates  $\overline{u'w'}$  (Figure 13a) exhibit a larger scatter than  $\overline{v'w'}$  (Figure 13b). The covariance between sonic temperature  $\theta'$  and the fluctuating vertical component  $w'$  (Figure 13c), and the Obukhov length  $L$  (Figure 13d) demonstrate good correlation and small scatter. The vertical velocity component is used in the numerator and denominator when calculating  $L$ . Thus, the lower scatter may be attributed to the larger uncertainties associated with component  $w$  cancelling each other to some degree. Sample  $s_5$ , depicted in pink, consistently exhibits the highest scatter. This sample has the shortest duration, lasting only 10 min, which is at least 4.7 min shorter than all other samples. Thus, sample  $s_5$  may be more prone to errors associated with insufficient sampling of the largest turbulent eddies.

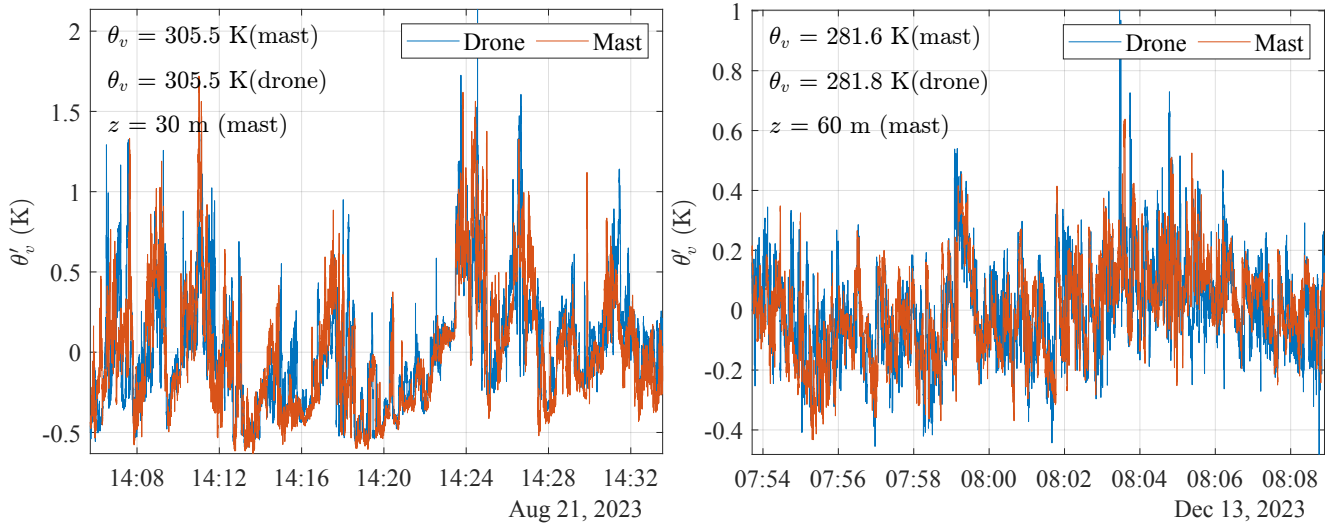


**Figure 10.** Time series of the sonic temperature for samples  $s_1$  (left panel) and  $s_7$  (right panel) measured by the drone-mounted anemometer and the mast-mounted sonic at a height of 30 m and 60 m above the ground, respectively.

The discrepancies between the vertical velocity spectral densities estimated by the mast-mounted sonic anemometers and by the drone are explored in more detail through the ratios  $S_w/S_u$  and  $S_v/S_u$ , following the method presented in Section 4.1. Chamecki and Dias (2004) states that if the spectral ratio trends towards 4/3 without actually reaching it, this could indicate that isotropy in the inertial subrange has not been achieved within the examined frequency range, a situation typically occurring in stable stratification flow conditions. In this study, the spectral ratios reached a plateau for all ten samples, albeit not always with a value of 4/3. This suggests that the atmospheric conditions were favorable to the observation of local isotropy, but that flow distortion may have been present.

Figure 14 shows that at lower wind speeds, SAMURAI-S may provide accurate estimations of the vertical velocity components as  $\langle S_w/S_u \rangle$  is fairly close to 1.33 for  $\bar{u} < 6 \text{ m s}^{-1}$ . As an opposite trend, SAMURAI-S overestimates this ratio as wind speed increases, whereas the mast data display ratios between 1.0 and 1.25. While these mast data may be closer to the expected ratio of 1.33 compared to the SAMURAI-S, they could still represent an underestimation of up to 20% of the vertical fluctuating component. Similar observations apply for the ratios  $\langle S_v/S_u \rangle$ . For  $\bar{u} > 6 \text{ m s}^{-1}$ , the ratio  $\langle S_w/S_u \rangle$  exceeds the expected value of 1.33 in drone measurements.

The recorded data in this study mainly represent stable or near-neutral atmospheric conditions, as  $\zeta$  was positive for most flights. An exception is found in  $s_1$ , collected under unstable atmospheric conditions ( $\zeta = -0.46$ ) and features the closest agreement between the drone and mast-mounted sensors. Further research is necessary to determine whether convective conditions consistently enhance the performance of the drone-based setup described in this paper or if these observations can be generalized across different turbulence intensities and atmospheric conditions. In addition, it is necessary to point out that

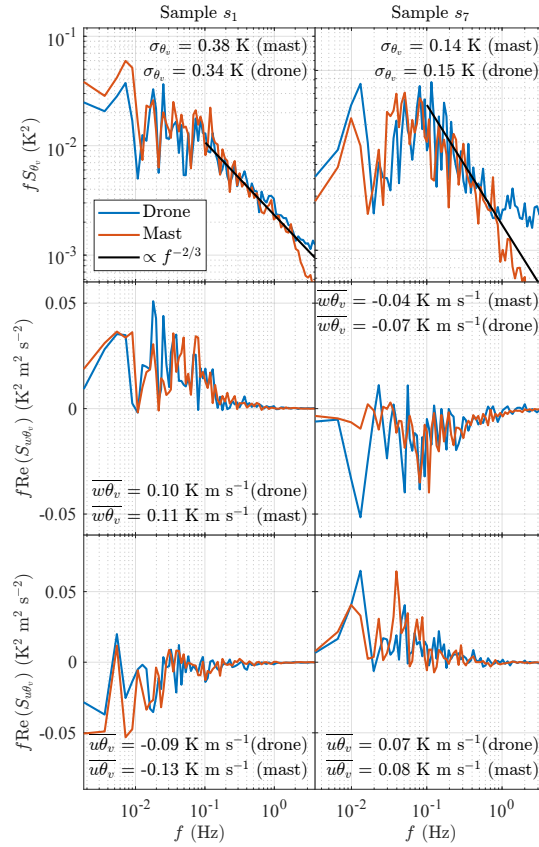


**Figure 11.** PSD estimates of the sonic temperature fluctuations and associated CPSD with the vertical and the along wind component for both the flying sonic anemometer and the one mounted on the mast 30 m above the ground for samples  $s_1$  (left panels) and at 60 m above ground for samples  $s_7$  (right panels).

except for  $s_1$ , the wind originates from a sector of  $280^\circ$  to  $310^\circ$  for all other flights. The limited number of samples and the range of stability and wind directions prevent drawing broader conclusions concerning systematic effects.

## 6 Conclusions

This study presents a pioneering effort in atmospheric research, focusing on using a research-grade 3D sonic anemometer mounted 18 m under a drone to observe turbulence. The goal was to assess the effectiveness of drone-mounted sonic anemometers as a versatile tool for turbulence measurement, challenging traditional methods that mount the same sensor on masts or towers. A notable aspect of this research was the application of a dynamic motion compensation algorithm that accounts for the motion and tilt of the sonic anemometer while the drone hovered above the location of interest. This study also employed the double-rotation method for static tilt correction.

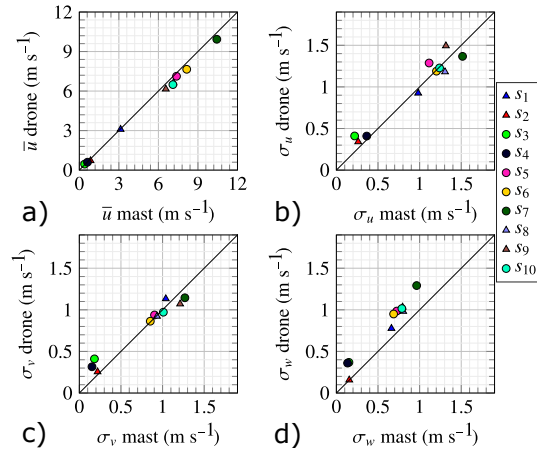


**Figure 12.** Mean wind speed and standard deviation of the three velocity components for the mast- and the drone-mounted sonic anemometer across the ten validation samples. Circle markers indicate measurements from the mast at 30 m above the surface, while triangle markers correspond to measurements at 60 m.

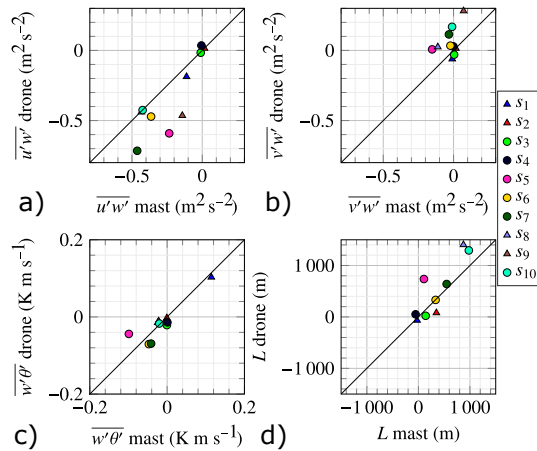


**Figure 13.** Turbulence covariance and Obukhov length for the ten validation samples, as measured by the mast- and the drone-mounted sonic anemometer. Circle markers represent measurements from the mast at 30 m above the surface, whereas triangle markers signify measurements at 60 m.

Data collection took place during the Models and Observations for Surface Atmosphere Interactions (MOSAI) campaign in France. The methodology included a comparative analysis between conventional mast-mounted 3D sonic anemometers at 30 m and 60 m above ground and the drone-mounted anemometer. This comparison focused on mean flow and turbulence characteristics, cross-covariance, and auto- and cross-spectral densities of velocity fluctuations. Our findings indicate that the drone-mounted anemometer effectively captures detailed turbulence measurements. Although there is good agreement regarding the along-wind and cross-wind flow when comparing the drone and mast data, the drone-based observations consistently

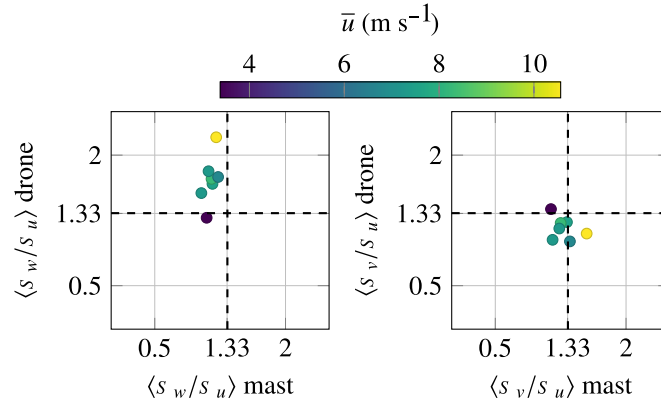


**Figure 14.** Quadrant analysis for the frequency-averaged spectral ratios  $\langle S_w/S_u \rangle$  (left panel) and  $\langle S_v/S_u \rangle$  (right panel) with  $fr > 2$  and  $fr < 10$  between the mast and drone-based measurements for different mean wind speeds. The notation  $\langle \rangle$  denotes an average over frequency bins. Only samples with a mean wind speed above  $2 \text{ m s}^{-1}$  are included.

overestimate the fluctuations of the vertical wind across all flights performed. This overestimation increases as the wind speed increases, calling for further analysis under a broader range of wind conditions.

For the drone-mounted anemometer, the spectral ratio  $S_w/S_u$  was up to 63% larger than the local isotropy hypothesis predicted in the inertial subrange. However, it was also observed that the mast-mounted anemometer could significantly underestimate the vertical turbulence component, with a spectral ratio  $S_w/S_u$  that was up to 22% lower than predicted by the local isotropy hypothesis in the inertial subrange.

The sonic temperature and the Obukhov length estimated by both sensors were also investigated. The comparison provides a positive and encouraging overall picture, with good agreement between the mast and drone measurements. The only exception is the shortest sample (10 min compared to at least 15 min for all others), which exhibits markedly divergent behaviour compared to its mast-measured counterpart.

Overall, the findings underscore the reliability of the drone-mounted anemometer in recording the along-wind velocity component and its potential complementarity with mast-mounted sonic anemometers and Scanning Doppler wind lidar for the study of atmospheric three-dimensional turbulence.

*Data availability.* Data underlying the results presented in this paper can be obtained from the authors upon reasonable request.

## Appendix A: Trasformation Matrix

The transformation matrix  $R(\phi, \theta, \psi)$  is defined as

$$R(\phi, \theta, \psi) = [R_3(\phi)R_2(\theta)R_1(\psi)]^T$$



where

$$R_1(\psi) = \begin{pmatrix} \cos \psi & \sin \psi & 0 \\ -\sin \psi & \cos \psi & 0 \\ 0 & 0 & 1 \end{pmatrix},$$

$$420 \quad R_2(\theta) = \begin{pmatrix} \cos \theta & 0 & -\sin \theta \\ 0 & 1 & 0 \\ \sin \theta & 0 & \cos \theta \end{pmatrix},$$

$$R_3(\phi) = \begin{pmatrix} 1 & 0 & 0 \\ 0 & \cos \phi & \sin \phi \\ 0 & -\sin \phi & \cos \phi \end{pmatrix}.$$

*Author contributions.* Conceptualization was done by EC, JR, MG, and STK. The methodology was developed by EC, JR, MG, and STK. Project management was handled by JR. The experiment was conducted by JR, MG, and STK. Data analysis was performed by EC, MG, and STK. The original draft was prepared by EC, JR, MG, and STK, and the review and editing were done by EC, JR, MG, and STK.

*Competing interests.* The authors declare no conflict of interest.

*Disclaimer.* The authors declare that they have no known competing financial interests or personal relationships that could have appeared to influence the work reported in this paper.

*Acknowledgements.* This research is funded by the Marie Skłodowska Curie Innovation Training Network Train2Wind (H2020-MSCA-ITN-2019, Grant number 861291). MOSAI project is funded by French ANR (Agence Nationale de la Recherche) and takes advantage of long-term measurements acquired at ACTRIS (Aerosol, Clouds and Trace Gases Research Infrastructure) and ICOS (Integrated Carbon Observation System) instrumented sites. AERIS data center is in charge of the data distribution and of the website of MOSAI project. (<https://mosai.aeris-data.fr>). We want to thank Tor Olav Kristensen for supporting the initial phase of this project. We also extend our sincere gratitude to everyone involved in the MOSAI campaign, whose help has been invaluable in the success of this study.



## 435 References

- Abichandani, P., Lobo, D., Ford, G., Bucci, D., and Kam, M.: Wind Measurement and Simulation Techniques in Multi-Rotor Small Unmanned Aerial Vehicles, *IEEE Access*, 8, 54 910–54 927, <https://doi.org/10.1109/ACCESS.2020.2977693>, 2020.
- Alaoui-Sosse, S., Durand, P., Medina, P., Pastor, P., Lothon, M., and Cernov, I.: OVLI-TA: An Unmanned Aerial System for Measuring Profiles and Turbulence in the Atmospheric Boundary Layer, *Sensors*, 19, 581, <http://www.mdpi.com/1424-8220/19/3/581>, 2019.
- 440 Båserud, L., Reuder, J., Jonassen, M. O., Kral, S. T., Paskyabi, M. B., and Lothon, M.: Proof of concept for turbulence measurements with the RPAS SUMO during the BLLAST campaign, *Atmospheric Measurement Techniques*, 9, 4901–4913, <https://www.atmos-meas-tech.net/9/4901/2016/>, 2016.
- Beard, R. W. and McLain, T. W.: *Small Unmanned Aircraft: Theory and Practice*, Princeton University Press, Princeton, United States, 2012.
- Busch, N. E. and Panofsky, H. A.: Recent spectra of atmospheric turbulence, *Quarterly Journal of the Royal Meteorological Society*, 94, 445 132–148, 1968.
- Calmer, R., Roberts, G. C., Preissler, J., Sanchez, K. J., Derrien, S., O, and apos;Dowd, C.: Vertical wind velocity measurements using a five-hole probe with remotely piloted aircraft to study aerosol–cloud interactions, *Atmospheric Measurement Techniques*, 11, 2583–2599, <https://www.atmos-meas-tech.net/11/2583/2018/>, 2018.
- Canut, G., Couvreur, F., Lothon, M., Legain, D., Piguet, B., Lampert, A., Maurel, W., and Moulin, E.: Turbulence fluxes and vari-  
 450 ances measured with a sonic anemometer mounted on a tethered balloon, *Atmospheric Measurement Techniques*, 9, 4375–4386, <https://doi.org/10.5194/amt-9-4375-2016>, 2016.
- Chamecki, M. and Dias, N.: The local isotropy hypothesis and the turbulent kinetic energy dissipation rate in the atmospheric surface layer, *Quarterly Journal of the Royal Meteorological Society: A journal of the atmospheric sciences, applied meteorology and physical oceanography*, 130, 2733–2752, 2004.
- 455 Cheynet, E., Jakobsen, J., and Reuder, J.: Velocity Spectra and Coherence Estimates in the Marine Atmospheric Boundary Layer, *Boundary-Layer Meteorology*, 169, <https://doi.org/10.1007/s10546-018-0382-2>, 2018.
- Cheyne, E., Jakobsen, J. B., and Snæbjörnsson, J.: Flow distortion recorded by sonic anemometers on a long-span bridge: Towards a better modelling of the dynamic wind load in full-scale, *Journal of Sound and Vibration*, 450, <https://doi.org/10.1016/j.jsv.2019.03.013>, 2019.
- Fernando, H. and Weil, J.: Whither the stable boundary layer? A shift in the research agenda, *Bulletin of the American Meteorological*  
 460 *Society*, 91, 1475–1484, 2010.
- Flem, A. A., Ghirardelli, M., Kral, S. T., Cheynet, E., Kristensen, T. O., and Reuder, J.: Experimental Characterization of Propeller-Induced Flow (PIF) below a Multi-Rotor UAV, *Atmosphere*, 15, <https://doi.org/10.3390/atmos15030242>, 2024.
- Foken, T.: 50 years of the Monin-Obukhov similarity theory, *Boundary-Layer Meteorology*, 119, 431–447, <https://doi.org/10.1007/s10546-006-9048-6>, 2006.
- 465 Foken, T., Aubinet, M., and Leuning, R.: The Eddy Covariance Method, pp. 1–19, Springer Netherlands, Dordrecht, ISBN 978-94-007-2351-1, [https://doi.org/10.1007/978-94-007-2351-1\\_1](https://doi.org/10.1007/978-94-007-2351-1_1), 2012.
- Ghirardelli, M., Kral, S. T., Müller, N. C., Hann, R., Cheynet, E., and Reuder, J.: Flow Structure around a Multicopter Drone: A Computational Fluid Dynamics Analysis for Sensor Placement Considerations, *Drones*, 7, 467, <https://doi.org/10.3390/drones7070467>, 2023.
- González-Rocha, J., De Wekker, S. F. J., Ross, S. D., and Woolsey, C. A.: Wind Profiling in the Lower Atmosphere from Wind-Induced  
 470 Perturbations to Multicopter UAS, *Sensors*, 20, <https://doi.org/10.3390/s20051341>, 2020.



- Guillermo, P. H., Daniel, A. V., and Eduardo, G. E.: CFD Analysis of two and four blades for multirotor Unmanned Aerial Vehicle, in: 2018 IEEE 2nd Colombian Conference on Robotics and Automation (CCRA). IEEE, pp. 1–6, 2018.
- Hobby, M. J.: Turbulence Measurements from a Tethered Balloon, Ph.D. thesis, University of Leeds, 2013.
- Hofsäß, M., Bergmann, D., Denzel, J., and Cheng, P. W.: Flying UltraSonic–A new way to measure the wind, *Wind Energy Science Discussions*, pp. 1–21, 2019.
- Jin, L., Ghirardelli, M., Mann, J., Sjöholm, M., Kral, S. T., and Reuder, J.: Rotary-wing drone-induced flow – comparison of simulations with lidar measurements, *Atmospheric Measurement Techniques*, 17, 2721–2737, <https://doi.org/10.5194/amt-17-2721-2024>, 2024.
- Kaimal, J. C. and Finnigan, J. J.: *Atmospheric Boundary Layer Flows: Their Structure and Measurement*, Oxford university press, 1994.
- Kaimal, J. C., Wyngaard, J., Izumi, Y., and Coté, O.: Spectral Characteristics of Surface-Layer Turbulence, *Quarterly Journal of the Royal Meteorological Society*, 98, 563–589, 1972.
- Lei, Y. and Cheng, M.: Aerodynamic performance of a Hex-rotor unmanned aerial vehicle with different rotor spacing, *Measurement and Control*, 53, 711–718, 2020.
- Lei, Y., Ye, Y., and Chen, Z.: Horizontal wind effect on the aerodynamic performance of coaxial Tri-Rotor MAV, *Applied Sciences*, 10, 8612, 2020.
- Li, Z., Pu, O., Pan, Y., Huang, B., Zhao, Z., and Wu, H.: A Study on Measuring the Wind Field in the Air Using a multi-rotor UAV Mounted with an Anemometer, *Boundary-Layer Meteorology*, 188, 1–27, 2023.
- Lothon, M., Lohou, F., Pino, D., Couvreur, F., Pardyjak, E. R., Reuder, J., Vilà-Guerau de Arellano, J., Durand, P., Hartogensis, O., Legain, D., Augustin, P., Gioli, B., Lenschow, D. H., Faloon, I., Yagüe, C., Alexander, D. C., Angevine, W. M., Bargain, E., Barrié, J., Bazile, E., Bezombes, Y., Blay-Carreras, E., van de Boer, A., Boichard, J. L., Bourdon, A., Butet, A., Campistron, B., de Coster, O., Cuxart, J., Dabas, A., Darbieu, C., Deboudt, K., Delbarre, H., Derrien, S., Flament, P., Fourmentin, M., Garai, A., Gibert, F., Graf, A., Groebner, J., Guichard, F., Jiménez, M. A., Jonassen, M., van den Kroonenberg, A., Magliulo, V., Martin, S., Martinez, D., Mastroiello, L., Moene, A. F., Molinos, F., Moulin, E., Pietersen, H. P., Pignatelli, B., Pique, E., Román-Cascón, C., Rufin-Soler, C., Saïd, F., Sastre-Marugán, M., Seity, Y., Steeneveld, G. J., Toscano, P., Traullé, O., Tzanos, D., Wacker, S., Wildmann, N., and Zaldei, A.: The BLLAST field experiment: Boundary-Layer Late Afternoon and Sunset Turbulence, *Atmospheric Chemistry and Physics*, 14, 10931–10960, <https://doi.org/10.5194/acp-14-10931-2014>, 2014.
- Mahrt, L.: Stably stratified atmospheric boundary layers, *Annual Review of Fluid Mechanics*, 46, 23–45, 2014.
- Mansour, M., Kocer, G., Lenherr, C., Chokani, N., and Abhari, R. S.: Seven-Sensor Fast-Response Probe for Full-Scale Wind Turbine Flowfield Measurements, *Journal of Engineering for Gas Turbines and Power*, 133, 081 601, <http://gasturbinespower.asmedigitalcollection.asme.org/article.aspx?articleid=1428610>, 2011.
- Marcq, S. and Weiss, J.: Influence of sea ice lead-width distribution on turbulent heat transfer between the ocean and the atmosphere, *The Cryosphere*, 6, 143–156, 2012.
- Mauder, M., Cuntz, M., Drüe, C., Graf, A., Rebmann, C., Schmid, H. P., Schmidt, M., and Steinbrecher, R.: A strategy for quality and uncertainty assessment of long-term eddy-covariance measurements, *Agricultural and Forest Meteorology*, 169, 122–135, <https://doi.org/10.1016/j.agrformet.2012.09.006>, 2013.
- Mauder, M., Foken, T., Aubinet, M., and Ibrom, A.: Eddy-covariance measurements, in: *Springer Handbook of Atmospheric Measurements*, pp. 1473–1504, Springer, 2021.



- Midjiyawa, Z., Cheynet, E., Reuder, J., Ágústsson, H., and Kvamsdal, T.: Potential and challenges of wind measurements using met-masts in complex topography for bridge design: Part II – Spectral flow characteristics, *Journal of Wind Engineering and Industrial Aerodynamics*, 211, 104585, <https://doi.org/10.1016/j.jweia.2021.104585>, 2021.
- 510 Monin, A. S. and Obukhov, A. M.: Basic laws of turbulent mixing in the surface layer of the atmosphere, *Contrib. Geophys. Inst. Acad. Sci. USSR*, 151, e187, 1954.
- Natalie, V. A. and Jacob, J. D.: Experimental Observations of the Boundary Layer in Varying Topography with Unmanned Aircraft, in: *AIAA Aviation 2019 Forum*, American Institute of Aeronautics and Astronautics, <https://doi.org/10.2514/6.2019-3404>, 2019.
- Ogawa, Y. and Ohara, T.: Observation of the turbulent structure in the planetary boundary layer with a kytoon-mounted ultrasonic anemometer system, *Boundary-Layer Meteorology*, 22, 123–131, <https://doi.org/10.1007/BF00128060>, 1982.
- 515 Olesen, H. R., Larsen, S. E., and Højstrup, J.: Modelling velocity spectra in the lower part of the planetary boundary layer, *Boundary-Layer Meteorology*, 29, 285–312, 1984.
- Palomaki, R. T., Rose, N. T., van den Bossche, M., Sherman, T. J., and Wekker, S. F. D.: Wind estimation in the lower atmosphere using multirotor aircraft, *Journal of Atmospheric and Oceanic Technology*, 34, 1183–1191, 2017.
- 520 Peña, A., Dellwik, E., and Mann, J.: A method to assess the accuracy of sonic anemometer measurements, *Atmospheric Measurement Techniques*, 12, 237–252, 2019.
- Porté-Agel, F., Bastankhah, M., and Shamsoddin, S.: Wind-turbine and wind-farm flows: A review, *Boundary-Layer Meteorology*, 174, 1–59, 2020.
- Prudden, S., Fisher, A., Mohamed, A., and Watkins, S.: A flying anemometer quadrotor: Part 1, 7th International Micro Air Vehicle Conference and Competition - Past, Present and Future, 2016.
- 525 Rautenberg, A., Schön, M., zum Berge, K., Mauz, M., Manz, P., Platis, A., van Kesteren, B., Suomi, I., Kral, S. T., and Bange, J.: The Multi-Purpose Airborne Sensor Carrier MASC-3 for Wind and Turbulence Measurements in the Atmospheric Boundary Layer, *Sensors*, 19, 2292, <https://doi.org/10.3390/s19102292>, 2019.
- Segales, A. R., Greene, B. R., Bell, T. M., Doyle, W., Martin, J. J., Pillar-Little, E. A., and Chilson, P. B.: The CopterSonde: an insight into the development of a smart unmanned aircraft system for atmospheric boundary layer research, *Atmospheric Measurement Techniques*, 13, 2833–2848, <https://doi.org/10.5194/amt-13-2833-2020>, 2020.
- 530 Shelekhov, A., Afanasiev, A., Shelekhova, E., Kobzev, A., Tel'minov, A., Molchunov, A., and Poplevina, O.: Using small unmanned aerial vehicles for turbulence measurements in the atmosphere, *Izvestiya, Atmospheric and Oceanic Physics*, 57, 533–545, 2021.
- Shimura, T., Inoue, M., Tsujimoto, H., Sasaki, K., and Iguchi, M.: Estimation of Wind Vector Profile Using a Hexarotor Unmanned Aerial Vehicle and Its Application to Meteorological Observation up to 1000 m above Surface, *Journal of Atmospheric and Oceanic Technology*, 35, 1621 – 1631, <https://doi.org/10.1175/JTECH-D-17-0186.1>, 2018.
- 535 Taylor, P. C., Hegyi, B. M., Boeke, R. C., and Boisvert, L. N.: On the Increasing Importance of Air-Sea Exchanges in a Thawing Arctic: A Review, *Atmosphere*, 9, <https://doi.org/10.3390/atmos9020041>, 2018.
- Thielicke, W., Hübert, W., Müller, U., Eggert, M., and Wilhelm, P.: Towards accurate and practical drone-based wind measurements with an ultrasonic anemometer, *Atmospheric Measurement Techniques*, 14, 1303–1318, 2021.
- 540 Tieleman, H. W.: Universality of velocity spectra, *Journal of Wind Engineering and Industrial Aerodynamics*, 56, 55–69, 1995.
- Van der Hoven, I.: Power spectrum of horizontal wind speed in the frequency range from 0.0007 to 900 cycles per hour, *Journal of Meteorology*, 14, 160–164, 1957.



- 545 Veers, P., Dykes, K., Lantz, E., Barth, S., Bottasso, C. L., Carlson, O., Clifton, A., Green, J., Green, P., Holttinen, H., et al.: Grand challenges in the science of wind energy, *Science*, 366, eaau2027, 2019.
- Welch, P.: The use of fast Fourier transform for the estimation of power spectra: a method based on time averaging over short, modified periodograms, *IEEE Transactions on Audio and Electroacoustics*, 15, 70–73, 1967.
- Wetz, T., Wildmann, N., and Beyrich, F.: Distributed wind measurements with multiple quadrotor unmanned aerial vehicles in the atmospheric boundary layer, *Atmospheric Measurement Techniques*, 14, 3795–3814, 2021.
- 550 Wildmann, N. and Wetz, T.: Towards vertical wind and turbulent flux estimation with multicopter uncrewed aircraft systems, *Atmospheric Measurement Techniques*, 15, 5465–5477, 2022.
- Wildmann, N., Hofsäß, M., Weimer, F., Joos, A., and Bange, J.: MASC – a small Remotely Piloted Aircraft (RPA) for wind energy research, *Advances in Science and Research*, 11, 55–61, <http://www.adv-sci-res.net/11/55/2014/>, 2014a.
- Wildmann, N., Ravi, S., and Bange, J.: Towards higher accuracy and better frequency response with standard multi-hole probes in turbulence measurement with remotely piloted aircraft (RPA), *Atmospheric Measurement Techniques*, 7, 1027–1041, <http://www.atmos-meas-tech.net/7/1027/2014/>, 2014b.
- 555 Wilson, T. C., Brenner, J., Morrison, Z., Jacob, J. D., and Elbing, B. R.: Wind Speed Statistics from a Small UAS and Its Sensitivity to Sensor Location, *Atmosphere*, 13, <https://www.mdpi.com/2073-4433/13/3/443>, 2022.
- Witte, B., Singler, R., and Bailey, S.: Development of an Unmanned Aerial Vehicle for the Measurement of Turbulence in the Atmospheric Boundary Layer, *Atmosphere*, 8, 195, <http://www.mdpi.com/2073-4433/8/10/195>, 2017.
- 560 Wu, L. and Qiao, F.: Wind Profile in the Wave Boundary Layer and Its Application in a Coupled Atmosphere-Wave Model, *Journal of Geophysical Research: Oceans*, 127, 1–15, <https://doi.org/10.1029/2021JC018123>, 2022.